Response of small sea ice floes in regular waves: a comparison of numerical and experimental results

Wei Bai[1, 2, *], Tong Zhang[2] and David J. McGovern[3]

1. School of Computing, Mathematics and Digital Technology, Manchester Metropolitan University, Chester Street, Manchester M1 5GD, UK

2. Department of Civil and Environmental Engineering, National University of Singapore, Kent Ridge, Singapore 117576, Singapore

3. Department of Civil, Environmental & Geomatic Engineering, University College London, Gower Street, London, WC1E 6BT, UK

Abstract

In severe seas ice floes can gain significant kinetic energy presenting a hazard to offshore structures and shipping. A numerical investigation is presented to investigate the kinematic response of sea ice floes in waves. The results are compared against available experimental data. The surge, heave and drift velocity are analysed for various different ice floe shapes using the potential flow model HydroSTAR® and the viscous flow CFD model OpenFOAM®. The results show relative wavelength (λ normalised with floe length L_c) λ/L_c strongly influences heave and surge, with a heave resonance occurring at $\lambda/L_c = 8$ for the cubic floe not being correspondingly observed for the square floe. The heave Response Amplitude Operator (RAO) is found to increase with floe thickness with a resonance occurring when relative thickness $b/L_c \geq 0.5$. Shape is observed to be less important than thickness. At small values of λ/L_c the floe is observed to move forward over the whole wavelength resulting in its drift displacement. Both vertical velocity relative to theoretical particle velocity V_y/V_p and ratio of forward and backward velocities show resonance at $\lambda/L_c = 8$. Comparing with experimental data, the linear analysis using HydroSTAR® overestimates the heave and surge RAOs. OpenFOAM®, however, appears to provide a much better agreement with the experimental data indicating viscosity plays an important role in floe kinematics.

Key words: Ice floe; Dynamic response; Linear analysis; Computational fluid dynamics; Experimental study

* Corresponding author.
E-mail address: w.bai@hotmail.com (W. Bai).

1. Introduction

The trend in the decline of Arctic sea ice is predicted to lead to an ice-free Arctic Ocean by 2040 (ACIA, 2004). Such seasonal reduction in sea ice coverage may open the North West Passage and Northern Sea Routes to shipping, greatly reducing the journey time between the Pacific and Atlantic Oceans. Additionally, according to a USGS (United States Geological Survey) survey between 13 and 30% of the world's untapped oil and gas are thought to be located beneath the Arctic Ocean (USGS, 2008). The reduction in ice coverage is cause for increased interest in exploiting these reserves.

The Arctic is a particularly harsh environment and hazards to offshore and shipping operations include that of sea ice interactions (Thompson and Rogers, 2014). The loss of ice coverage will increase fetch and, in low concentrations, such as stretches of ocean adjacent to but not within the Marginal Ice Zone (MIZ), motions of a sea ice floe (floating ice block which is not attached to land) that is small with respect the dominant wavelength (λ) will be driven by ocean waves and become significant in severe seas. The analysis of the problem is similar to that of a thin, free-floating body, and a detailed review is given in McGovern and Bai (2014a). In the case of small fragments of sea ice, i.e., up to tens of meters in size and much smaller than the dominant wavelengths, the floe is essentially non-compliant (Meylan and Squire, 1994, 1996, McGovern and Bai, 2014a). In such a case flexural response of the floe is negligible and radiation damping is dominant. The floes may still cover a large region of many kilometres in length, but will be found in all different sizes down to small floes. Such small floes even in the MIZ are sensitive to full six degrees of freedom of motions from wave forcings (Frankenstein et al., 2001). Indeed such motions have been measured in the field on isolated glacial ice bergs of a variety of sizes (Wadhams et al., 1983). Understanding the kinematic response of a small ice floe in wave is, therefore, key to properly addressing the potential hazard that such a floe may have to offshore operations and shipping in the Arctic.

Due to its significance in cold regions engineering practice, there has been extensive research on drift motions of small ice floes. Initially, researchers focused more on the derivation of theoretical or semi-theoretical models to solve the simplified ice problems. For example, Rumer et al. (1979) extended the Morison's equation to calculate the drift motion of small floating object in a gravity wave field. Shen and Ackley (1991) used a one-dimensional model to study collisions between ice floes and herding using the

slope-sliding model proposed in Rumer et al. (1979). Shen and Zhong (2001) found that wave reflection has a profound effect on the drift pattern. Even for a very small reflection coefficient, the floating object can stop its propagation after some time. This trapping phenomenon depends on the added mass and drag coefficients. Marchenko (1999) independently derived a similar slope-sliding theory as in Rumer et al. (1979). Grotamaack & Meylan (2006) related the two theories in Marchenko (1999), Shen and Zhong (2001) and identified an error in the derivation of Rumer et al. (1979). Recently, Huang et al. (2016) presented an improved analytical solution to the drift of small rigid floating objects of arbitrary shapes under regular waves.

Apart from the two comprehensive reviews in Squire et al. (1995) and Squire (2007) where a large amount of research on the interaction of sea ice and ocean waves in the MIZ have been summarised, many experiments and theoretical studies have been carried out to study the response of small floating objects in waves. Arunachalam et al. (1987) analyzed the short term motion of icebergs in linear waves both theoretically and experimentally. Lever et al. (1988a, 1988b) and Huang et al. (2011) studied different factors which can affect the motion and drift velocity of small icebergs experimentally. However, it can be seen that most attention has focused on glacial icebergs, which are now well understood. Attention, including the works of Meylan and Squire (1994, 1996) and Meylan (2002), has focused on the flexural response of thin floating bodies in waves. Of interest here is how the compliant properties of the floes affect floe kinematic and reflection response.

More recently, Montiel et al. (2013a, 2013b) presented measurements of the oscillatory motions of thin plastic disk in regular waves, and compared the measurements with predictions of the potential flow model. Bennetts and Williams (2015) presented measured surge, heave and pitch motions of a solitary wooden disk at a subset of the incident wave frequencies and amplitudes used for their tests. Their model was based on a combined potential flow and thin plate theory, and the assumption of linear motions. Both a low-concentration array in which discs were separated by approximately one disc diameter in equilibrium, and a high-concentration array in which adjacent discs were almost touching in equilibrium, were considered in their experiments. Meylan et al. (2015a) presented measurements of the surge, heave and pitch motions of a thin plastic disk as a function of λ. They showed that the model predictions in their study are accurate for incident λ approximately greater than two times floe diameter. Meylan et al. (2015b) tested the motions of

87 two different plate models with distinct material properties in regular waves by using the thin plate model.
88 The results indicated that the motions of floes are essentially linear.

89 In order to further understand kinematics of ice floes in water waves, McGovern and Bai (2014a)
90 conducted an experiment in a wave flume to investigate in detail the kinematic and dynamic response of ice
91 floes, their drift velocity, the influence of body geometry, thickness and other parameters. They concluded
92 that the ice floe's motion can be affected by its own properties such as shape and thickness and also the wave
93 properties such as wavelength. Additional discussion on ice floe interaction and impact characteristics with a
94 single fixed vertical cylinder was given in McGovern and Bai (2014b). They studied the effect of a single
95 cylinder on the upstream, near-cylinder, impact and post impact kinematics and velocities of floes of various
96 shapes in a variety of wave conditions. This paper is, therefore, the follow-up of our previous work on ice
97 floe kinematics. As the experimental data presented in McGovern and Bai (2014a) was not sufficiently
98 validated due to the lack of published data in the public domain, one aim of the present paper is to reproduce
99 the physical experiment numerically, so that the accuracy of both our experiment and the present numerical
100 study in the kinematics of ice floes can be firmly verified by the comprehensive comparison between the
101 numerical and experimental results. Also, different numerical tools are compared and recommendations are
102 made.

103 However, the literature review shows that CFD work on the kinematics of ice floes in water waves is very
104 rare. Therefore, identifying a suitable numerical tool for the ice floe problem is another aim of the present
105 paper. Two different numerical tools are chosen to carry out the numerical simulation: the linear analysis
106 based on the potential flow theory by the software HydroSTAR® and the computational fluid dynamic (CFD)
107 simulation based on the viscous flow theory by the open source tool OpenFOAM®. OpenFOAM®, with the
108 advantage of being free and open source, has been adopted to solve many problems in coastal and offshore
109 engineering. In the study of Higuera et al. (2013), the OpenFOAM® was adopted to simulate several coastal
110 processes such as wave breaking and wave interaction with obstacle. Chen et al (2014) also used this CFD
111 tool to study wave interaction with a vertical cylinder. Both of these two studies indicated that the
112 OpenFOAM® is accurate and promising. After testing three validation cases, Morgan et al. (2010, 2011)
113 concluded that OpenFOAM® may potentially be a very useful tool for researchers and engineers in coastal
114 and offshore engineering. To simulate water waves, Jacobsen et al. (2012) extended OpenFOAM® with a
115 wave generation and absorption method. Furthermore, Higuera et al. (2013a, 2013b) implemented the

specific boundary conditions for realistic wave generations and presented a robust three-dimensional, two-phase numerical model for practical applications in coastal engineering.

2. Experimental study

2.1 Experiment setup

The experimental set-up is described in detail in McGovern and Bai (2014a) and as such, is given here in brief. The flume used is the 32 m long 2 m wide wave flume situated in the Hydraulic Engineering Laboratory at the National University of Singapore. An effective absorption beach was located at the end of the flume. Extensive testing during the construction of the flume showed that the beach reflects < 5% of incident wave height, and this was confirmed by additional testing before the current experimental campaign in McGovern and Bai (2014a). Sea ice models of various shapes are formed from paraffin wax (density ρ = 890 kg m^{-3}). The kinematic response of the models in regular waves is measured using a PhaseSpace Improv motion tracking system, see Fig. 1a. This system tracks the full six-degrees-of-freedom of motion of the floe models in the test section. Free surface elevation is recorded using four resistance-type wave gauges up and downstream of the test section (Fig. 1b). The system consisted of 8 cameras mounted on a frame around the test section supported by the flume walls. The cameras are able to resolve the LED to 0.1mm at a distance of 5m. The LEDs were positioned at equidistant points from each corner of the ice model. The system was calibrated using a calibration wand on which LEDs are fixed at known distance apart. The accuracy of the system is rated at 1% of the distance between the cameras and the measured LED (see McGovern and Bai, 2014a for more details).

Fig. 1 a) Image of a floe model with attached LED lights undergoing testing in regular waves and b) a schematic diagram of the flume.

2.2 Data processing

145 Raw data obtained in the experiments is the time series record of displacement in the *x* and *y* directions.
146 The solid line in Fig. 2 shows the raw data of *x* displacement, which cannot be used directly for the analysis
147 of surge motion due to the presence of the drift motion. According to the engineering practice, the surge
148 motion refers to the periodically oscillating component in the *x* displacement. Therefore, to obtain the surge
149 motion the effect of drift motion should be separated from the time series record. It should be noted that due
150 to the different processing procedure, the surge motion defined in McGovern and Bai (2014a) is slightly
151 different to the conventional definition of surge motion widely adopted in engineering practice, since the
152 drift motion is not completely removed from the results of surge motion. Here, to be in line with the
153 conventional definition of surge motion, the mean value of *x* displacement at each time instant is calculated
154 by averaging the displacement around this time instant over one wave period. The oscillating surge motion is
155 eventually obtained by removing the mean at each time instant from the measured signal. By using this
156 processing procedure, the oscillating component can be separated from the motion in the *x* direction, as
157 shown by the dashed line in Fig. 2, which can be defined as the surge motion of moving body. The same
158 approach will also be adopted in the following sections to process the numerical results.
159
160
161 Fig. 2 An example of *x* displacement trace in experiment and corresponding surge motion after processing
162
163 In addition, since the large drift motion is a specific phenomenon associated with ice floes in waves, the
164 drift velocity is a key physical property that is of great engineering significance when studying ice impact
165 problems (Huang et al. 2011). Generally, the constant drift velocity in the quasi-steady state can be
166 computed by two approaches (Huang et al. 2011). One is to obtain the instantaneous mean velocity within
167 one wave period based on an up-crossing method that is widely used in analyzing irregular waves. In this
168 method, the period-averaged mean drift velocity is a function of time, and can be calculated by dividing the
169 horizontal displacement between two neighboring peaks by the wave period. The other method is to
170 calculate the mean drift velocity in the quasi-steady stage by determining the slope of a best-fitting linear
171 trend line, which is adopted in this study. For the purpose of demonstration, Fig. 3 shows the *x* displacement
172 trace for a typical case in the experiment, and the corresponding best-fitting linear trend line from 15s to 35s
173 marked by a thick solid line. The information regarding the performance of the approach is also shown in a

small table embedded in the figure. The drift velocity V_d can be easily determined by calculating the slope of the best-fitting line. In the case shown in the figure, the drift velocity V_d is 0.05947m/s.

Fig. 3 An illustration of determination of drift velocity V_d using the best-fitting linear line approach.

3. Linear numerical analysis

There exist various numerical models ranging from the simplified linear potential flow model to the more complete computational fluid dynamic simulations, which are available for the numerical simulation of response of ice floes in water waves. However, each numerical model has its own advantages and disadvantages due to various assumptions made and inherent natures of the model. In this study, we mainly focus on two popular numerical models, and evaluate the performance of these two models.

3.1 Linear diffraction/radiation method

The fluid is assumed to be incompressible and inviscid, and the motion irrotational. The water wave problem can be formulated in terms of a velocity potential $\phi(x, y, z, t)$, which satisfies Laplace's equation within the fluid domain surrounding the ice floe (Chen et al. 2015),

$$\nabla^2\phi = 0\,, \tag{1}$$

and is subject to the boundary conditions applied on the ice floe surfaces given as:

$$\frac{\partial\phi}{\partial n} = \mathbf{V}_n\,, \tag{2}$$

where n is the normal unit vector pointing out of the fluid domain, and $\boldsymbol{V}_n$ the normal velocity component of the solid surfaces. On the water surface, the first order boundary condition is

$$\frac{\partial^2\phi}{\partial t^2} + g\frac{\partial\phi}{\partial z} = 0\,, \tag{3}$$

where g is the acceleration due to gravity. In addition, a suitable radiation condition on the outer boundary should be imposed to avoid the wave reflection from the far-field boundary.

This boundary value problem has been successfully solved in many widely used commercial software packages. In this study, the software package HydroSTAR® is adopted, which provides a complete solution of the first order problem of wave diffraction and radiation. The main output includes the wave forces and moments, wave elevation and dynamic response of floating bodies. As for the problem of ice floes in water waves investigated in the present study, this linear analysis tool is applied to simulate a cube of length 20cm, and a square plate of length 30cm and thickness 5cm, in order to examine the capability of the linear analysis for this thin ice floe problem. The assumption of kL_c = O(1) is applicable for the potential flow model, where k is the wave number and L_c is the typical body length. After the mesh convergence test, the numbers of panels in the x, y and z directions are chosen to be 8, 8 and 8 for the cube in the calculation, while the numbers of panels for the square plate are 18, 18 and 6. Due to the symmetry of the computational domain, only a quarter of the body is considered in the calculation, so that there are in total 80 and 189 panels on the cube and square plate surfaces, respectively.

3.2 Numerical results and discussions

Our experimental results reveal that ice floe kinematics can be affected by incident wave height H and wavelength λ. However, in the linear analysis RAO (Response Amplitude Operator) of bodies is independent with incident wave height. We, therefore, can only study the influence of wavelength on the dynamic response of ice floes in waves. To make a direct comparison with our experiments, the wavelength is varied from 1.0m to 3.0m for the cube and from 0.6m to 3.0m for the square plate, as in the experiments. The linear analysis can directly provide the surge and heave RAOs, where the effect of drift is excluded. The numerical results are compared with the experimental data measured at the wave steepness H/λ of 0.02 for the cube and 0.044 for the square plate, as shown in Fig. 4 and Fig. 5 respectively. From the comparison of surge and heave RAOs of the cube as a function of relative wavelength λ/L_c, it can be seen that the surge RAO is in acceptable agreement, but the numerical simulation over-predicts the heave response by four times that of the experimental measurement at the peak frequency around λ/L_c = 7 - 9. Here, L_c is defined as the length of the edge in horizontal plane for the square plate and the length of the edge for the cube respectively. For the square plate in Fig. 5, the numerical results reveal that the linear analysis seems to over-predict both the surge and heave RAOs. An unreasonable peak appears in both the surge and heave RAOs at about λ/L_c = 3,

whose value exceeds 1. Therefore, in the regime where λ/L_c is between 2 to 4, the linear analysis can be considered to provide inaccurate results for the square plate considered here.

Fig. 4 Comparison of surge (a) and heave (b) RAOs of cube between the linear analysis and experiment

Fig. 5 Comparison of surge (a) and heave (b) RAOs of square plate between the linear analysis and experiment

Generally speaking, although with the similar trend, the linear analysis by HydroSTAR® is not able to provide good agreement with the experimental results, especially in the resonance range for the heave motion of the cube. The over-prediction of the numerical simulation is mainly due to the neglection of fluid viscosity in the potential flow model, which is verified later in Figs. 9 and 10 by the numerical results obtained using the viscous flow solver OpenFOAM® where the viscosity of fluid is considered. It is unsurprising that the results obtained by the linear potential flow analysis cannot agree with the experimental results well, as it is known that this theory is only valid for certain range of body size relative to wavelength. The only damping in the potential flow model is due to radiation damping, while as in the experimental case, viscous damping appears to play a more significant role in accurately predicting the dynamic responses. In addition to the assumptions made in the potential flow model, the linearization might be another source of error in the linear analysis. At the same time, as the commercial software HydroSTAR® can only provide the results in the frequency domain, which means the information about the displacement trace and the drift velocity that are the significant physical properties when studying ice floes in water waves, is missing. The advantage of the linear analysis is efficiency; the simulation can finish in a very short period of time. For a particular case, full RAO can be obtained on a normal workstation in 10 minutes when 500 wave frequencies are considered. However, to obtain more accurate numerical results with detailed information, a computational fluid dynamic simulation with the nonlinearity and fluid viscosity being taken into account is necessary.

4. Computational fluid dynamic (CFD) simulation

4.1 Mathematical formulation

The governing equations for viscous flows are the Reynolds averaged Navier-Stokes equations (Ferziger and Peric, 2012) within the domain surrounding the ice floe:

$$\frac{\partial \rho}{\partial t} + \frac{\partial}{\partial x_j}\left(\rho u_j\right) = 0\,, \tag{4}$$

$$\frac{\partial}{\partial t}\left(\rho u_i\right) + \frac{\partial}{\partial x_j}\left(\rho u_j u_i\right) = -\frac{\partial p}{\partial x_i} + \frac{\partial}{\partial x_j}\left[\mu_e\left(\frac{\partial u_j}{\partial x_i} + \frac{\partial u_i}{\partial x_j}\right)\right] + \rho g_i\,, \tag{5}$$

where x_j (j = 1, 2, 3) represents the coordinate components, u_j is the fluid velocity, p is the pressure, ρ is the fluid density. $\mu_e = \mu + \mu_f$, where μ is the fluid viscosity and μ_f is the turbulent eddy viscosity. In order to close the above governing equations, the two-equation k-ε turbulence model is adopted to simulate the turbulent flows:

$$\frac{\partial}{\partial t}\left(\rho k\right) + \frac{\partial}{\partial x_j}\left(\rho u_j k\right) = \frac{\partial}{\partial x_j}\left[\left(\mu + \frac{\mu_f}{\delta_k}\right)\frac{\partial k}{\partial x_j}\right] + P_k - \rho\varepsilon\,, \tag{6}$$

$$\frac{\partial}{\partial t}\left(\rho \varepsilon\right) + \frac{\partial}{\partial x_j}\left(\rho u_j \varepsilon\right) = \frac{\partial}{\partial x_j}\left[\left(\mu + \frac{\mu_f}{\delta_\varepsilon}\right)\frac{\partial \varepsilon}{\partial x_j}\right] + C_1 P_k \frac{\varepsilon}{k} - \rho C_2 \frac{\varepsilon^2}{k}\,, \tag{7}$$

$$P_k = \mu_f\left(\frac{\partial u_j}{\partial x_i} + \frac{\partial u_i}{\partial x_j}\right)\frac{\partial u_i}{\partial x_j}\,, \tag{8}$$

where $\mu_f = C_\mu \rho k^2/\varepsilon$, k is the turbulent kinetic energy, ε is the turbulent energy dissipation rate, δ_k and δ_ε are the turbulent Schmidt numbers. The constants in the turbulence model are set as C_μ = 0.09, C_1 = 1.44, C_2 = 1.92, δ_k = 1.0 and δ_ε = 1.33.

Volume of Fluid method (VOF) (Hirt and Nichols, 1981) is adopted to capture the air-water interface (the free water surface). In this method, the fraction of water volume existing in each computational element (known as the volume fraction) is advected by solving the following transport equation:

$$\frac{\partial \alpha}{\partial t} + \frac{\partial}{\partial x_j}\left(u_j \alpha\right) = 0\,, \tag{9}$$

where α is the volume fraction of water. The volume fraction is used as the weighting factor to predict the fluid properties in each computational element,

$$\rho = \alpha\rho_w + (1-\alpha)\rho_a, \tag{10}$$

$$\mu = \alpha\mu_w + (1-\alpha)\mu_a, \tag{11}$$

where the subscripts *w* and *a* represent the corresponding fluid property of water and air respectively. It should be noted that on the body surface, the non-slip boundary condition is applied.

4.2 Numerical implementation of OpenFOAM®

The CFD calculations are carried out using an open source CFD software, OpenFOAM® (Open Source Field Operation and Manipulation) which was first released in 2004. OpenFOAM® is essentially a C++ library that is used to create solvers for various fluid flow problems. OpenFOAM® comes with a great number of solvers but its open source nature can also enable users write their own solvers. Jacobsen et al. (2012) developed a solver, called Waves2Foam, to deal with the wave generation and wave-structure interaction problems. While this solver doesn't include the dynamic mesh utility in OpenFOAM® and as a result cannot deal with floating bodies. In the present study, Waves2Foam is coupled with the dynamic mesh function embedded in another OpenFOAM® solver, called WaveDyMFoam, such that the moving body problems can be solved in the frame of Waves2Foam.

Three different types of floes are considered in the CFD calculations using OpenFOAM®: the first two are the cube and square plate that have been defined before in the linear analysis, and the last geometry is a regular triangle plate of length 30cm and thickness 5cm. The present study mainly investigates the effect of wavelength on ice floe kinematics, by varying the wavelength from about 0.6m to 3.0m for all these three geometries. In the simulation of the cube, the wave steepness is set to $H/\lambda = 0.02$, as used in the experiments. However, the wave steepness H/λ remains to be 0.044 for both the square and triangle plates, which was also adopted in the experiments for the same geometries. Various wave heights are also tested for the square plate with the same wavelength to study the influence on the drift velocity. The effect of ice floe thickness is also studied by a series tests for the square plate. Therefore, in total 54 test cases are run using OpenFOAM®.

In the numerical simulations, BlockMesh, a mesh type in OpenFOAM® which is very suitable for regular geometries, is used to discretize the computational domain for the cube and square plate, where the total numbers of elements are 400,000 and 432,000 respectively. For the triangle plate, because of the relatively

irregular shape of the body SnappyHexMesh, another mesh type in OpenFOAM® which is more robust for irregular geometries, is used and 571,802 elements are adopted in the simulations. It should be noted that a coarser mesh of 200,000 elements and a finer mesh of 800,000 elements have also been tested for the cube to validate the feature of mesh convergence (not shown here). The calculations at those three meshes reveal that the intermediate mesh of 400,000 elements and the finer mesh can provide very agreeable results that deviate from those obtained at the coarser mesh, indicating that the results presented below at the adopted mesh is convergent in terms of computational mesh. In addition, non-uniform mesh is used for all the three geometries with suitable mesh refinement around the free surface and body surface. With 400,000 elements, one simulation for a duration of 30s and a particular λ/L_c takes about 3 to 4 hours in OpenFOAM® using 8 computer processors. In this study, our main focus is on the global dynamic motion of bodies in waves, rather than the detailed turbulent flow structures. Therefore, no special consideration has been given to the treatment of flow boundary layer. In Fig. 6, an example mesh is shown for a floating square plate generated in OpenFOAM®. Table 1 shows the wave properties and model shapes of simulations in OpenFOAM®.

Fig. 6 The example mesh in OpenFOAM® for ice floe problem

Table 1 Summary of OpenFOAM® simulations

5. CFD and experimental Results

5.1 Time series of response

Time series of body response is a direct output in both the numerical simulation and experimental measurement. Fig. 7 shows the displacements in the x and y directions and the comparison between the numerical results and experimental data for the square plate over five wave periods after the steady state has been achieved. The steady state means both the surge and heave motions become periodic with constant amplitudes and the drift component becomes a fixed value in each wave period. In this case, the wavelength

λ = 3m and wave height H = 0.132m are considered. As shown in the figure, the ice floe experiences a periodic motion around the free surface in the y direction, whereas a clear drift can be observed although it also moves forwards and backwards periodically in the x direction. The comparison between the numerical results and experimental data shows that good agreement can be obtained for the surge and heave motions. To better demonstrate the body motion, the trajectory of the square plate moving in waves is shown in Fig. 8, from which we can see that the trajectory exhibits like a helix line rather than a closed line. The x displacement is periodic, but also involves a drifting component.

Fig. 7 Numerical and experimental results of time series of x (a) and y (b) displacements for the square plate

Fig. 8 Numerical result of trajectory of the square plate in waves

5.2 Effect of wavelength

In the tests of Lever et al. (1988a) for the iceberg motions, it was concluded that wavelength λ is a significant factor to influence the iceberg motions. In their experiments, four model geometries were adopted to study the effect of geometry on dynamic responses of icebergs. For a particular geometry, the influence of wavelength on body motions was also investigated. The results demonstrated that cylinder and cube models show a peak in the heave RAO at λ/ L_c = 6 and then tend to be around 1 at larger λ/L_c, while the sphere and trapezoid show no peak. In this study, we first present our numerical and experimental results of surge and heave RAOs for the cube and compare with the experimental data in Lever et al. (1988a), as shown in Fig. 9, to validate both our numerical model and experiment. For the 20cm cubic model, in McGovern and Bai (2014a) the test case was repeated for 6 times at each wave condition. The error bars of the experimental data are shown in Fig. 9, from which we can see that the errors of the experiments are small (less than 8%). We can also see from the figure that the surge and heave RAOs show different trend with the increase of relative wavelength λ/L_c for the cube. The surge RAO shows a constant increase with the wavelength, and after λ/L_c = 10 it approaches to 1, indicating the particle-like behavior of the ice floe. A peak appears in the heave RAO at around λ/L_c = 8; the heave motion decreases and tends to approach to 1 while increasing the

wavelength so that the cube behaves like a water particle, in both the numerical, present and Lever et al.'s experimental results. Schwerdtfeger (1980) used a rectangular iceberg and assumed the motion only in the vertical cross-section. The frequencies of both linear and angular oscillations of a floating iceberg in the vertical plane were shown to converge to a certain value with the increase of body size in the horizontal plane. It was found that the heave resonance of an iceberg with straight sides can be easily computed by assuming linear oscillations:

$$\left(\frac{\lambda}{h}\right)_{res} = 2\pi \frac{\rho_i}{\rho_w}\left(1+m_c\right), \tag{12}$$

where h is the thickness of the iceberg, m_c is the added mass coefficient in heave, ρ_i and ρ_w are the densities of ice and water respectively. The added mass coefficient for the cube in this case can be determined approximately by the formula $ma = 0.7\rho a^3$, as shown in Levins and Plunkett (1980). With this added mass coefficient, Eq. (12) shows that the heave resonance occurs at $\lambda/L_c = 9.7$ for the ice cube, which agrees with the numerical and experimental results shown in Fig. 9. This probably can also explain the lack of resonance in the heave for the square plate, as shown later. Eq. (12), at the same time, demonstrates that the thickness of the ice might be another important parameter, which will be further discussed later in detail.

Fig. 9 Comparison of surge (a) and heave (b) RAOs of the cube between the present numerical and experimental results, and the experimental data in Lever et al. (1988a)

Further observation of Fig. 9 reveals that the numerical result of surge motion is slightly different from the present experimental data, but closer to the data in Lever et al. (1988a). On the other hand, the heave motion in the numerical simulation experiences a larger peak compared to the experimental results, which may be due to the other damping influences (such as the surface roughness of the ice floe and the tank walls) in the experiments that cannot be taken into account in the numerical simulations. However, in general the present numerical simulation is able to provide accurate surge and heave RAOs, and the present experimental results are also in good agreement with numerical and Lever et al.'s experimental results.

Fig. 10 shows the surge and heave RAOs of the square plate in the present numerical simulation and physical experiment both with the wave steepness of $H/\lambda = 0.044$. As seen in the figure, it is distinguishable

from the cube case that there is no obvious peak observed in the heave RAO, but the surge RAO shows the similar characteristics with the cube case. It seems that the thickness of ice floe can affect the occurrence of the resonance phenomenon in the heave motion, which will be further discussed later. A small discrepancy can still be observed for λ/Lc <3 in both heave and surge RAOs, which may be attributed to the small wave height (about 2 cm) adopted in both the numerical and experimental studies. The wave height is small in order to retain a constant wave steepness for these short waves. This may cause errors in both the experiments and numerical simulations.

Fig. 10 Comparison of surge (a) and heave (b) RAOs of the square plate between the present numerical and experimental results

Furthermore, with considering the over-prediction and unrealistic peak in the linear analysis, as shown in Figs. 4 and 5, the CFD simulations can obtain much better results than the linear analysis, which is reflected by the better agreement with the experimental data, especially for the cube case. As discussed before, the over-prediction in the linear analysis is due to the linear nature and the omission of the fluid viscosity in the basic assumptions of the linear potential flow model. Therefore, compared to the CFD simulation, the linear analysis may not be very suitable in accurately modeling the motion of floating ice floes, even though it is very efficient in computer time.

At the same time, the physical experiment also observes the phenomenon of green water appeared when $\lambda/L_c < 5$ for the square plate. Green water is a quantity of water on the topside surface of body as a result of wave actions. The same green water is also noticed in the numerical simulations, whereas the critical value for the occurrence of this phenomenon is found to be around $\lambda/L_c = 4$. Fig. 11 shows the test cases with and without the green water observed at $\lambda/L_c = 4$ and $\lambda/L_c = 10$ respectively for the square plate at the wave steepness $H/\lambda = 0.044$. This green water effect may be one of the reasons for smaller surge and heave motions at smaller wavelengths. This phenomenon agrees with the findings in Skene et al (2015), where a theoretical model of overwash of a floating plate was presented and validated by laboratory experiments. They also showed that overwash generally occurs for waves with relatively short lengths. For the cases with

$\lambda/Lc < 4$, the relative error of the numerical simulation is larger and the reason has been discussed. For the cases with $\lambda/Lc > 4$, the relative error is less than 10% which means that the numerical results are reliable.

Fig. 11 The 3D free surface profile around the square plate for $\lambda/L_c = 4$ (a) with green water and $\lambda/L_c = 10$ (b) without green water

5.3 Effect of model shape

In the physical experiments, a series of ice floes with different shapes have been tested. In the CFD simulations, three model shapes are chosen to test the hydrodynamic performance of different bodies. For the influence of other body shapes, see McGovern and Bai (2014) for more details. The three body shapes chosen include the cube, square plate and triangle plate with streamline normal to one edge of the triangle. Fig. 12 shows the surge and heave RAOs of different body shapes obtained by both the numerical simulations and experiments. As seen in the figure, the surge motion presents an increasing trend with the increase of wavelength for all the three body shapes, and the numerical results are in good agreement with the experimental results. While for the heave RAO, results for different body shapes show great difference. For the cube, both the numerical and experimental results show a peak approximately at $\lambda/L_c = 8$, where the heave response can reach more than two times that of the wave height H. For the square and triangle plates, there is no obvious heave resonance. Generally, for all the three body shapes, the numerical results show the same trend with the experimental data. However, the numerical results seem to underestimate the heave RAO for both the square and triangle plates when the wavelength is small. For the cases with $\lambda/L_c < 4$， the relative errors of heave RAOs are relatively large especially for the cube and square plate. While for the cases with $\lambda/L_c > 4$, the relative errors of all the three models are less than 10% except for the cube with $\lambda/L_c = 8$. As for surge RAO, also the cube model shows the largest relative errors while the errors of all the three models are in a reasonable range.

Fig. 12 Comparison of surge (a) and heave (b) RAOs of three different body shapes between the present numerical and experimental results

5.4 Ice floe velocity

The velocity of ice floe is an important parameter when calculating ice impact force on structures by using the Morison equation (Wong and Sego, 1989). In the numerical simulation, the velocity of floating body can be exported directly, while in the physical experiment the velocity can be calculated from the time series of body displacement. Fig. 13 shows a comparison of time series of velocities in the x and y directions between the numerical and experimental results for the square plate with the wavelength λ = 3m and wave height H = 0.132m. It can be seen that the x velocity in the positive x direction is obviously larger than that in the negative direction, which indicates the occurrence of the body drift in the x direction. For the heave velocity, the maximum upward and downward velocities are approximately the same. When the steady state is reached, the maximum x and y velocities of the square plate predicted by the numerical simulation agree reasonably well with the experimental results.

Fig. 13 Time series of x (a) and y (b) velocities obtained by both the numerical simulation and experiment for the square plate with λ = 3m and H = 0.132m

Fig. 14 shows the x and y velocities, V_x and V_y, of the cube normalized by the corresponding theoretical water particle velocity V_p as a function of the relative wavelength λ/L_c. Here, V_x and V_y refer to the maximum velocities in the x and y directions respectively, and V_p is defined as:

$$V_{px} = \frac{H}{2}\sigma\frac{\cosh k(h+z)}{\sinh kh}\cos(kx-\sigma t) \tag{13}$$

$$V_{py} = \frac{H}{2}\sigma\frac{\sinh k(h+z)}{\sinh kh}\cos(kx-\sigma t) \tag{14}$$

As shown in the figure, the horizontal relative velocity V_x/V_p varies around 1 but shows no specific trend. The vertical relative velocity V_y/V_p demonstrates the same trend as in the heave RAO with a resonance

happened at approximately $\lambda/L_c = 8$. As for comparison, the numerical results agree with the experimental results well in V_y/V_p. However, V_x/V_p is smaller than the experimental results but with a similar trend. Furthermore, with the increase of λ/L_c the ratio of the horizontal positive and negative velocities is also shown in Fig. 15. As can be seen in the figure, the general trends of the numerical simulation and experiment are the same. The ratio shows a peak at $\lambda/L_c = 8$ and with the increase of λ/L_c, the ratio approaches an asymptotic value of 1.5.

Fig. 14 Comparison of numerical and experimental results of x (a) and y (b) velocities normalized by the theoretical water particle velocity for the cube

Fig. 15 Comparison of numerical and experimental results of the ratio of horizontal positive and negative velocities for the cube as a function of relative wavelength

For the cube, there is always a horizontal negative velocity at all the relative wavelengths investigated, which indicates that the cube moves forwards and backwards. However, for the square plate, the physical experiment shows that the horizontal negative velocity does not appear at small wavelengths when $\lambda/L_c < 5.3$. In this situation, the floe keeps moving forwards all the time without any backward motion. The same phenomenon is also observed in the present numerical simulation when $\lambda/L_c < 4$. This is because drift velocity becomes dominant when λ/L_c is small. Fig. 16 shows the numerical results of surge displacement for the square plate at $\lambda/L_c = 2$ and 5. With constant wave steepness, the larger wavelength implies that a higher wave was used in the simulation. Without the obvious backward velocity, the floe moves even faster at $\lambda/L_c = 2$ with a smaller wave height compared to that at $\lambda/L_c = 5$. This indicates that the drift velocity V_d does not necessarily increase with the wave height, but is affected more by the relative wavelength.

Fig. 16 Numerical result of displacement in the x direction for the square plate at $\lambda/L_c = 2$ and 5

To visualize the velocity in the domain, Fig. 17 shows the velocity field around the cube with the relative wavelength λ/L_c = 13 and wave height H = 0.052m at two time instants. In Fig. 17(a), the wave crest passes the cube at t = 10.3s, while the wave trough passes the cube at t = 10.9s in Fig. 17(b). When the wave crest passes, the velocity of most water particles around the body is pointing upwards and forwards so that the body also moves in that direction. However, when the wave trough passes, the velocity of most particles around the body is in the opposite direction, the body therefore moves downwards and backwards.

Figure. 17 Velocity field around the cube with λ/L_c = 13 and H = 0.052m at two time instants: (a) t = 10.3s and (b) t = 10.9s

5.5 Drift velocity

For a pure wave motion in fluid dynamics, the Stokes drift velocity is the average velocity when following a specific fluid parcel as it travels with the fluid flow. In the Lagrangian description, fluid parcels may drift far from their initial positions. The equation of the drift velocity is given as follow:

$$V_d = \frac{ga^2k^2 \cosh 2k(h+z)}{\omega \sinh 2kh}, \tag{15}$$

where a is the wave amplitude, ω is wave frequency.

According to Eq. (15), we can see that the solution is a quadratic function of the ka number. In the present study, the wavelength is constant at λ = 1.8m and the wave height is varied in order to achieve the desired range of ka numbers. Fig. 18 shows the numerical results of drift velocity for the square plate normalized by the wave celerity C as a function of ka number, together with the experimental results of both the present study for the same square plate and Huang et al. (2011) for the square plate of length 20cm and thickness 4.5cm. The drift velocity obtained by the Stokes wave theory is also included in the figure for clearer demonstration. Both the numerical and experimental results are slightly larger than the theoretical results as shown in Fig. 18 while they are generally in good agreement.

Fig. 18 Numerical result of drift velocity for the square plate and comparison with the experimental results of both the present study and Huang et al. (2011)

5.6 Effect of thickness

The present experimental data has shown that the floe thickness b has a dramatic effect on floe motions, especially in the heave direction. Fig. 19 shows the numerical and experimental results of heave RAO for the square plate with two different thicknesses, b = 5cm and b = 7.5cm. With increasing of λ/L_c, the heave RAO in both the numerical and experimental results seems to approach the value of 1. The floe with larger thickness has a larger heave response. The experimental results of the square plate with larger thickness also demonstrate that a heave resonance appears, although it is not very obvious. The numerical results seem to follow the same trend as the experimental data, but underestimate the heave RAO, as seen before. The square plate with thickness larger than 7.5cm is not further investigated in the experiment, as the aim of the experiment is to study the motion of sea ice floes with small thicknesses.

Fig. 19 Numerical and experimental heave RAOs for the square plate with two different thicknesses, b = 5cm and b = 7.5cm

As discussed before, the cube has shown an obvious heave resonance at about λ/L_c = 8. To further investigate this more numerical tests are run for a square plate of length 30cm with various thicknesses ranging from 5cm to 30cm, allowing for the systematic analysis of the effect of thickness as it changes gradually from a square plate to a cube. Fig. 20 shows the numerical result of heave response of those square plates with various floe thicknesses b. We can see from the figure that when the thickness $b \geq$ 15cm or the relative thickness $b/L_c \geq 0.5$, the heave RAO shows an obvious resonance, and with the thickness increasing, the heave resonance turns to be more and more significant.

Fig. 20 Numerical result of heave response of square plates with variable floe thicknesses b

6. Conclusion

A series of physical model tests are conducted to study response of small ice floes in regular water waves. Since this experiment addresses the research gap in the small ice floe kinematics, a numerical simulation of the same problem is necessary to validate the experimental results. Additionally, due to the high demand for resources and time consuming nature of the experiment, finding a reliable numerical tool is vital for the problem of small ice floes in water waves. To achieve this purpose, the linear analysis based on the potential flow model and the CFD simulation based on the viscous flow model are adopted and compared with the experimental data. Many distinct characteristics associated with kinematics of small ice floes in waves are identified in both the numerical and experimental studies.

The relative wavelength λ/L_c is found to have dramatic effect on the heave and surge RAOs. The heave resonance occurs for the cube at approximately the relative wavelength $\lambda/L_c = 8$, whereas for the square plate only an increasing trend is observed in the heave response. The present numerical simulation reveals that the heave RAO increases with the floe thickness, and the heave resonance appears at the relative thickness $b/L_c \geq 0.5$. The square and triangle plates with the same thickness b show minimal difference in the heave and surge motions. In the vertical direction the maximum upward and downward velocities are approximately the same. However, in the horizontal direction the maximum forward velocity is larger than the backward velocity and the difference causes the drift displacement. Both the vertical relative velocity V_y/V_p and the ratio of the forward and backward velocities in the horizontal direction V_+/V_- show a resonance at $\lambda/L_c = 8$. No backward velocity is observed when the relative wavelength λ/L_c is relatively small for the square plate; the floe moves forwards all the time. In addition to the comparison with the experimental results, to show the factor which affects the resonance, several additional cases other than that in the experiments are simulated to show the trend of body motions from non-resonance to resonance.

The linear results obtained by HydroSTAR® seem to overestimate the surge and heave RAOs especially for the cube when the resonance occurs in the range of $\lambda/Lc = 6$ to 9, probably because the nature of linear potential flow model adopted in HydroSTAR®. The inaccuracy can also be observed for the square plate considered here in the regime where $\lambda/Lc = 2$ to 4. In general, the open source CFD software OpenFOAM® can provide much better agreement with the experimental data than the linear analysis. Extensive CFD simulations and comparisons with the experimental data reveal that the numerical results obtained by OpenFOAM® are reasonably accurate, except for the underestimation of the heave RAO for the square plate.

593 The comparison shown in this study indicates that the fluid viscosity is an important parameter which cannot
594 be ignored at laboratory scale when investigating the response of small ice floes in water waves.
595
596 **References**
597

598 Arctic Climate Impact Assessment (ACIA) 2004. Impacts of a Warming Arctic. Cambridge University Press.
599 Arunachalam, V. M., Murrray, J. J. and Muggeridge, D. B. (1987). Short term motion analysis of icebergs in linear waves.
600 Cold Reg. Sci. Technol., 13, 247-258.
601 Bennetts, L. G. and Williams, T. D. (2015). Water wave transmission by an array of floating discs. Proceedings of the Royal
602 Society of London A: Mathematical, Physical and Engineering Sciences, 471(2173), 20140698.
603 Chen, X. B., Liu, H. X., & Duan, W. Y. (2015). Semi-analytical solutions to wave diffraction of cylindrical structures with a
604 moonpool with a restricted entrance. *Journal of Engineering Mathematics*, *90*(1), 51-66.
605 Blevins, R. D. and Plunkett, R. (1980). Formulas for natural frequency and mode shape. Journal of Applied Mechanics, 47,
606 461.
607 Ferziger, J. H. and Peric, M. (2012). Computational methods for fluid dynamics. Springer Science & Business Media.
608 Frankenstein, S., Loset, S. and Shen, H. H. (2001). Wave-ice interactions in the Barents sea marginal ice zone. Journal of Cold
609 Regions Engineering, 15 (2), 91-102.
610 Grotmaack, R. and Meylan, M. H. (2006). Wave forcing of small floating bodies. Journal of Waterway, Port, Coastal, and
611 Ocean Engineering, 132(3), 192-198.
612 Higuera, P., Lara, J. L. and Losada, I. J. (2013a). Realistic wave generation and active wave absorption for Navier–Stokes
613 models: Application to OpenFOAM®. Coastal Engineering, 71, 102-118.
614 Higuera, P., Lara, J. L. and Losada, I. J. (2013b). Simulating coastal engineering processes with OpenFOAM®. Coastal
615 Engineering, 71, 119-134.
616 Hirt, C. W. and Nichols, B. D. (1981). Volume of fluid (VOF) method for the dynamics of free boundaries. Journal of
617 computational physics, 39(1), 201-225.
618 Huang, G., Wing-Keung, A. L. and Huang, Z. (2011). Wave-induced drift of small floating objects in regular waves. Ocean
619 Eng., 38, 712- 718.
620 Huang, G., Huang, Z. H., & Law, A. W. (2016). Analytical Study on Drift of Small Floating Objects under Regular
621 Waves. *Journal of Engineering Mechanics*, *142*(6), 06016002.
622 Jacobsen, N. G., Fuhrman, D. R. and Fredsøe, J. (2012). A wave generation toolbox for the open-source CFD library:
623 OpenFoam®. International Journal for Numerical Methods in Fluids, 70(9), 1073-1088.

624 Lever, J. H., Attwood, D. and Sen, D. (1988a). Factors affecting the prediction of wave-induced iceberg motion. Cold Reg. Sci.
625 Technol., 15, 177-190.
626 Lever, J. H., Reimer, E. and Diemand, D. (1988b). A model study of the wave-induced motion of small icebergs and bergy bits.
627 J. Offshore Mech. Arct. Eng., 110, 101-107.
628 Lever, J. H., Klein, K., Mitchel, D. and Diemand, D. (1991). Wave-induced iceberg motion. Cold Regions Science and
629 Technology, 20, 11-23.
630 Marchenko, A. V. (1999). The floating behaviour of a small body acted upon by a surface wave. J. Appl. Math. Mech. 63(3),
631 471-478.
632 McGovern, D. J. and Bai, W. (2014a). Experimental study on kinematics of sea ice floes in regular waves. Cold Regions
633 Science and Technology, 103, 15-30.
634 McGovern, D. J. and Bai, W. (2014b). Experimental study of wave-driven impact of sea ice floes on a circular cylinder. Cold
635 Regions Science and Technology, 108, 36-48.
636 Meylan, M. H. (2002). Wave response of an ice floe of arbitrary geometry. J. Geophys. Res., 107 (C1), 3005.
637 Meylan, M. H., Yiew, L. J., Bennetts, L. G., French, B. J. and Thomas, G. T. (2015 a). Surge motion of an ice floe in waves:
638 comparison of theoretical and experimental models. Annals Glaciol., 56(69), 107-111.
639 Meylan, M. H., Bennetts, L. G., Cavaliere, C., Alberello, A. and Toffoli, A. (2015 b). Experimental and theoretical models of
640 wave-induced flexure of a sea ice floe. Physics of Fluids, 27(4), 041704.
641 Meylan, M. H. and Squire, V. A. (1994). The response of ice floes to ocean waves. J. Geophys. Res., 99 (C1), 899-900.
642 Meylan, M. H. and Squire, V. A., (1996). Response of a circular ice floe to ocean waves. J. Geophys. Res., 101 (C4), 8869–
643 8884.
644 Montiel, F., Bennetts, L. G., Squire, V. A., Bonnefoy, F. and Ferrant, P. (2013a). Hydroelastic response of floating elastic disks
645 to regular waves. Part 2: Modal analysis. J. Fluid Mech., 723, 629-652.
646 Montiel, F., Bonnefoy, F., Ferrant, P., Bennetts, L. G., Squire, V. A. and Marsault, P. (2013b). Hydroelastic response of floating
647 elastic disks to regular waves. Part 1: Wave tank experiments. J. Fluid Mech., 723, 604–628.
648 Morgan, G. and Zang, J. (2011). Application of OpenFOAM to coastal and offshore modelling. In: Proceedings of 26th
649 International Workshop of Water Wave and Floating Bodies, Athens, Greece.
650 Morgan, G., Zang, J., Greaves, D., Heath, A., Whitlow, C. and Young, J. (2010). Using the rasInterFoam CFD model for wave
651 transformation and coastal modelling. In: Proceedings of 32nd Conference on Coastal Engineering. Shanghai, China.
652 Rumer, R. R., Crissman, R. D. and Wake, A. (1979). Ice transport in great lakes. Great Lakes Environmental Research
653 Laboratory, National Oceanic and Atmospheric Administration, US Dept. of Commerce.
654 Schwerdtfeger.P. (1980). Iceberg oscillation and ocean waves. Ann. Glaciol, 1, 63-65.
655 Shen, H. H. and Ackley, S. F. (1991). A one-dimensional model for wave-induced ice-floe collisions. Annals Glaciol., 15, 87-
656 95.
657 Shen, H. H. and Zhong, Y. (2001). . J. Waterway, Port, Coastal, and Ocean Engineering, 127(6), 343–351.

Squire, V. A. (2007). Of ocean waves and sea-ice revisited. Cold Reg. Sci. Technol., 49, 110-133.

Squire, V. A., Dugan, J. P., Wadhams, P., Rottier, P. J. and Liu, A. K. (1995). Of ocean waves and sea-ice. Ann. Rev. of Fluid Mech., 27, 115-168.

Thomson, J. and Rogers, W. E. (2014). Swell and sea in the emerging Arctic Ocean. Geophysical Research Letters, 41(9), 3136-3140.

U.S. Geological Survey (USGS). (2008). Circum-Arctic Resource Appraisal: Estimates of Undiscovered Oil and Gas North of the Arctic Circle. U.S. Geological Survey Fact Sheet 2008-3049.

Wadhams, P., Kristensen, M. and Orheim, O. (1983). The response of Antarctic icebergs to ocean waves. Journal of Geophysical research, 88, 6053-6065.

Wong, T. T. and Sego, D. C. (1989). Design requirement for ice forces. Canadian Geotechnical Journal, 26(4), 524-535.

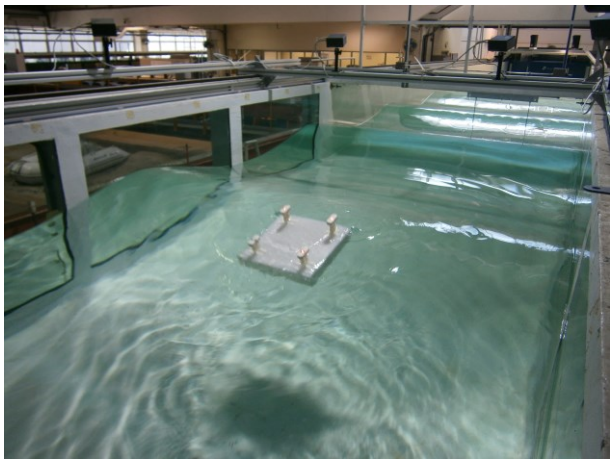

(a)

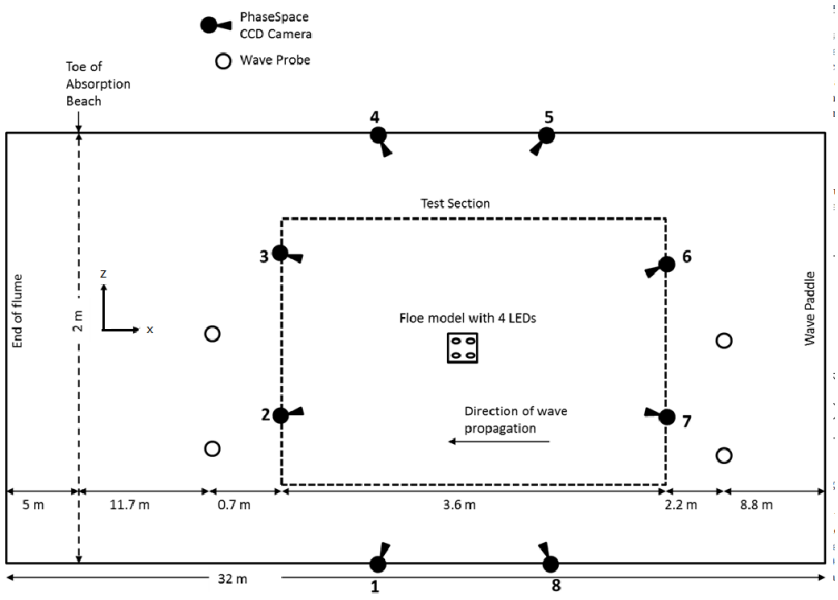

(b)

Fig. 1 a) Image of a floe model with attached LED lights undergoing testing in regular waves and b) a schematic diagram of the flume.

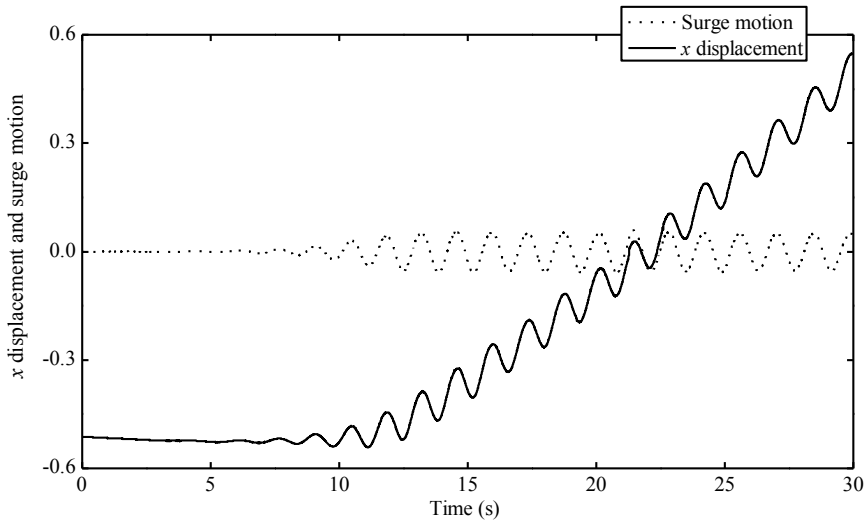

Fig. 2 An example of *x* displacement trace in experiment and corresponding surge motion after processing

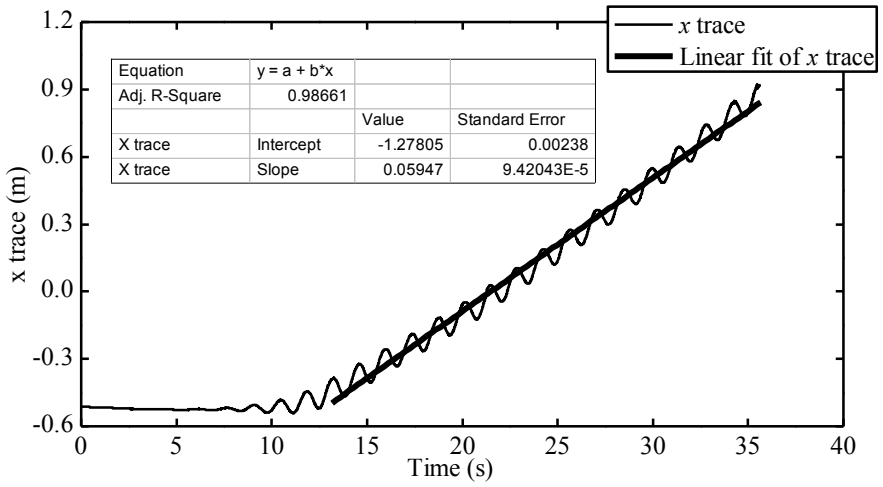

Fig. 3 An illustration of determination of drift velocity V_d using the best-fitting linear line approach.

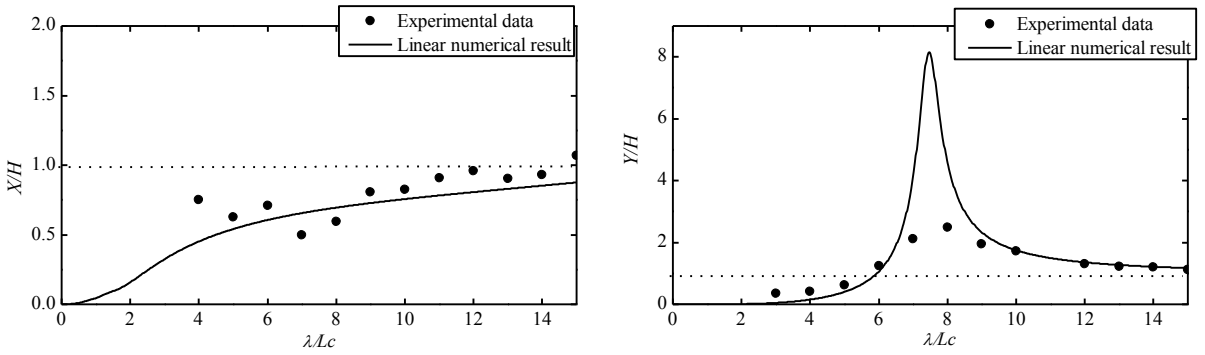

(a) Surge (b) Heave

Fig. 4 Comparison of surge (a) and heave (b) RAOs of cube between the linear analysis and experiment

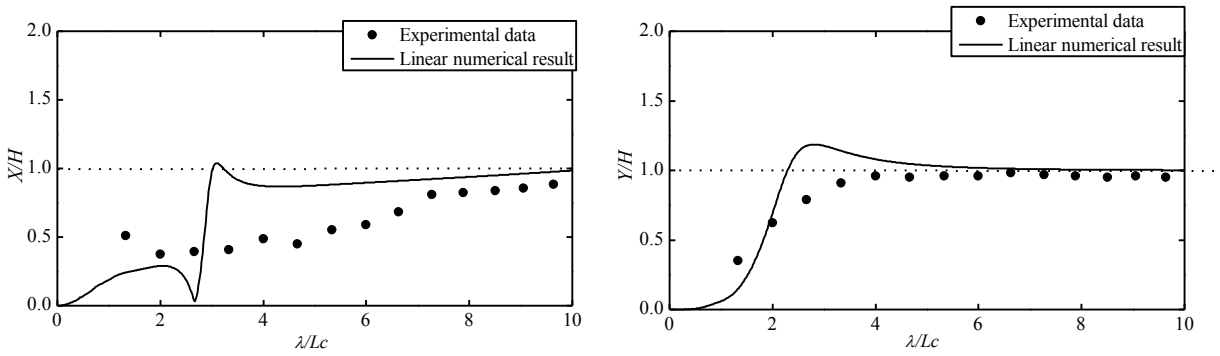

(a) Surge (b) Heave

Fig. 5 Comparison of surge (a) and heave (b) RAOs of square plate between the linear analysis and experiment

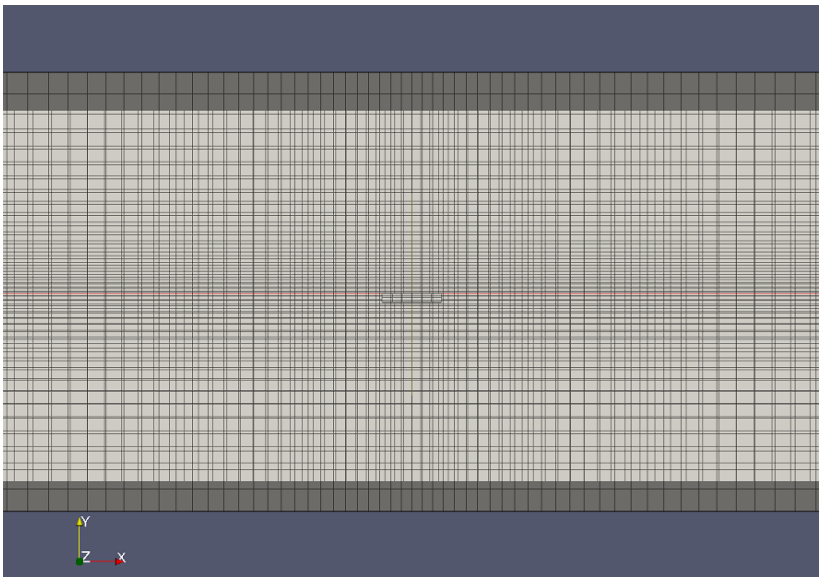

Fig. 6 The 3D view of an example mesh in OpenFOAM® for ice floe problem

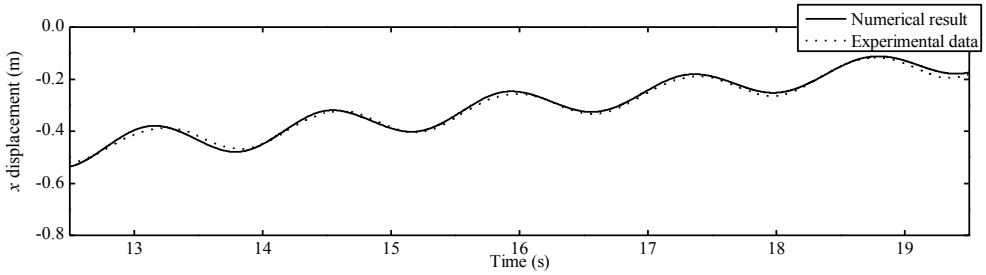

(a) *x* displacement

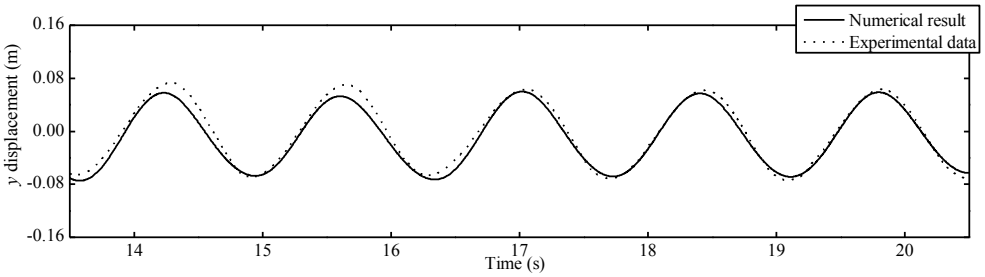

(b) *y* displacement

Fig. 7 Numerical and experimental results of time series of *x* (a) and *y* (b) displacements for the square plate

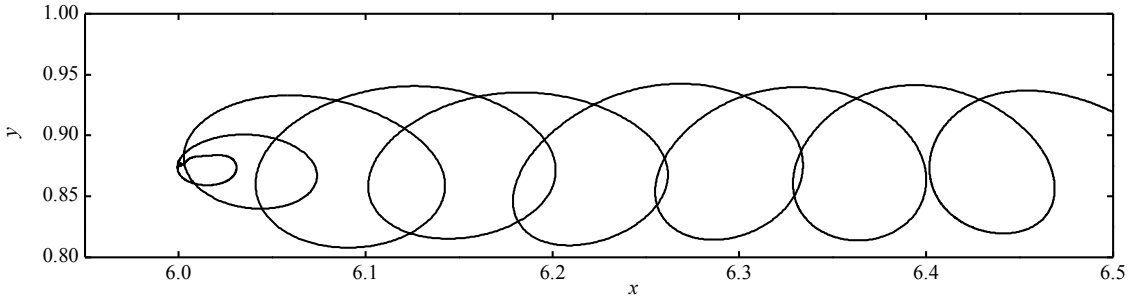

Fig. 8 Numerical result of trajectory of the square plate in waves

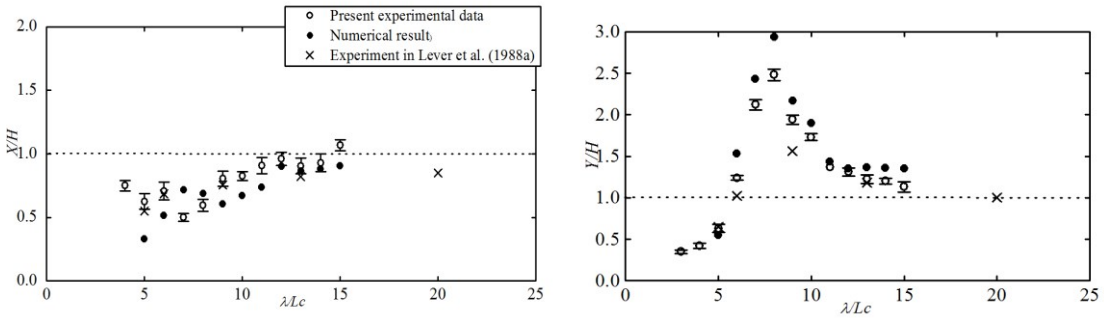

(a) Surge (b) Heave

Fig. 9 Comparison of surge (a) and heave (b) RAOs of the cube between the present numerical and experimental results, and the experimental data in Lever et al. (1988a)

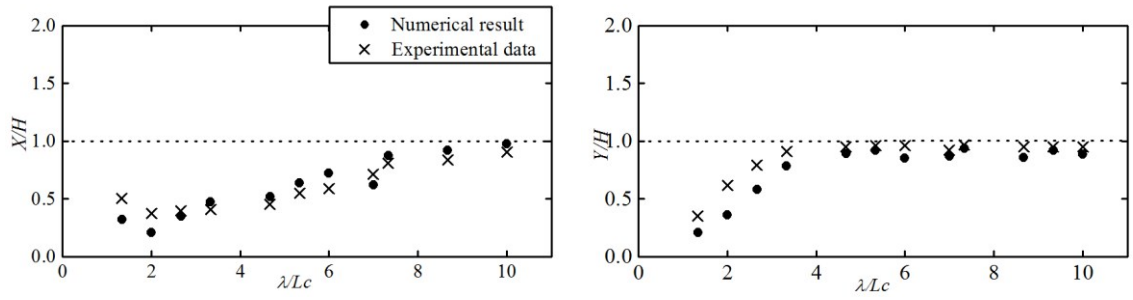

(a) Surge (b) Heave

Fig. 10 Comparison of surge (a) and heave (b) RAOs of the square plate between the present numerical and experimental results

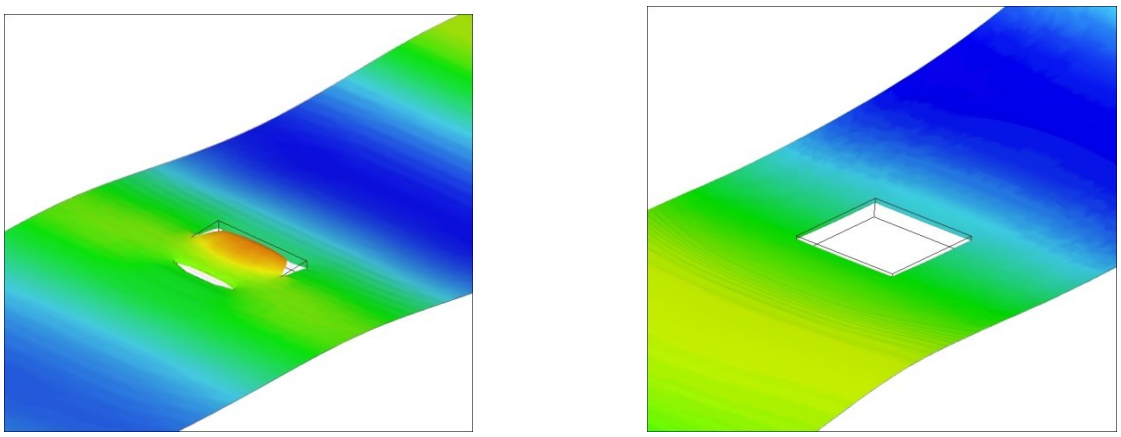

(a) $\lambda/L_c = 4$ (b) $\lambda/L_c = 10$

Fig. 11 The 3D free surface profile around the square plate for $\lambda/L_c = 4$ (a) with green water and $\lambda/L_c = 10$ (b) without green water

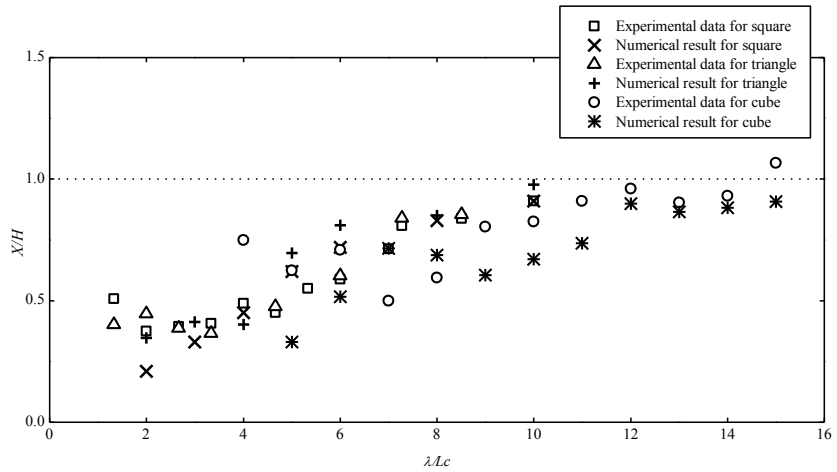

(a) Surge

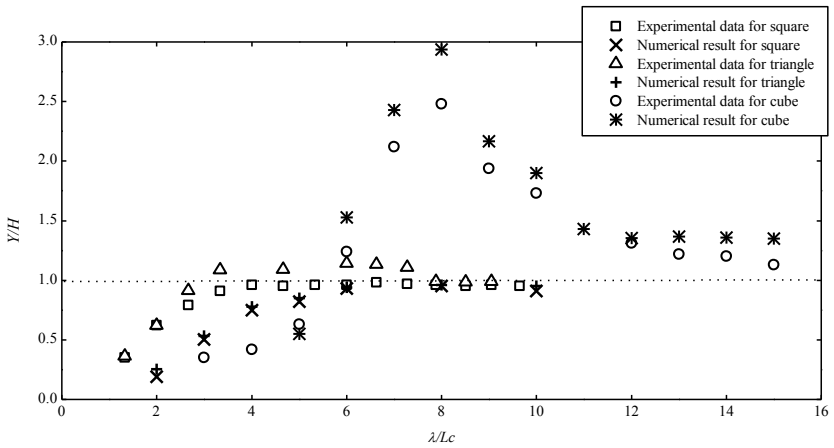

(b) Heave

Fig. 12 Comparison of surge (a) and heave (b) RAOs of three different body shapes between the present numerical and experimental results

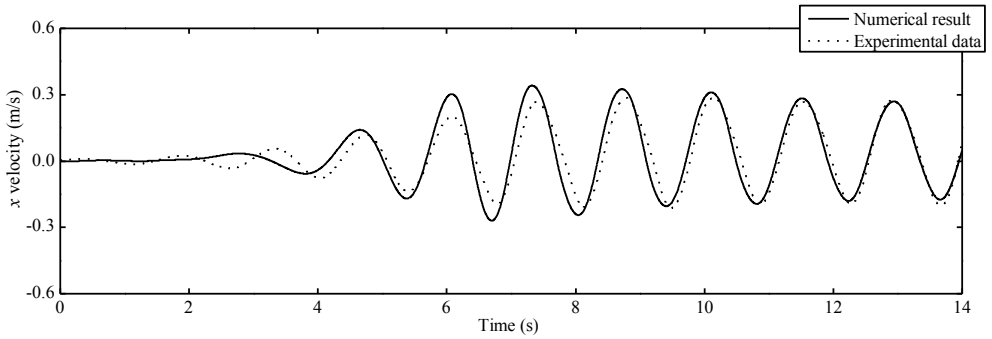

(a) *x* velocity

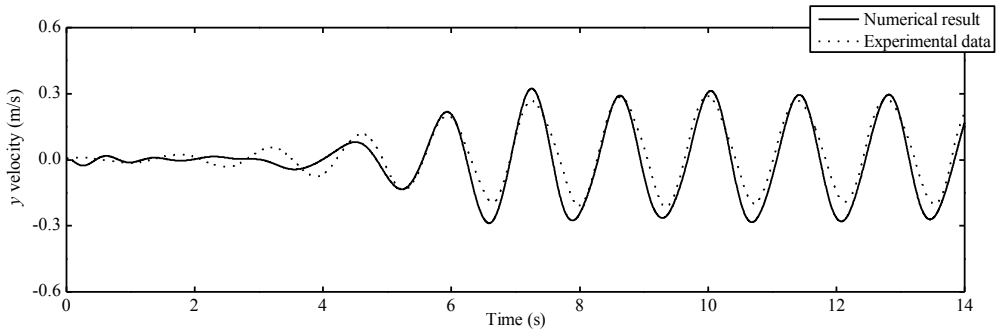

(b) *y* velocity

Fig. 13 Time series of *x* (a) and *y* (b) velocities obtained by both the numerical simulation and experiment for the square plate with λ = 3m and H = 0.132m

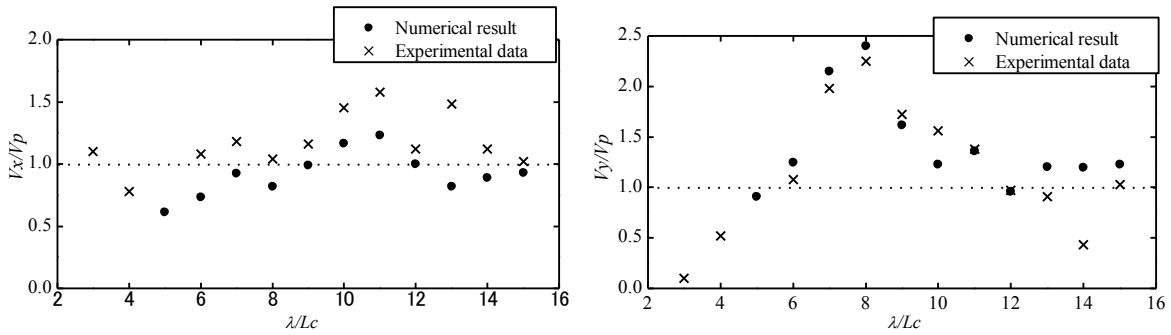

(a) *x* velocity (b) *y* velocity

Fig. 14 Comparison of numerical and experimental results of *x* (a) and *y* (b) velocities normalized by the theoretical water particle velocity for the cube

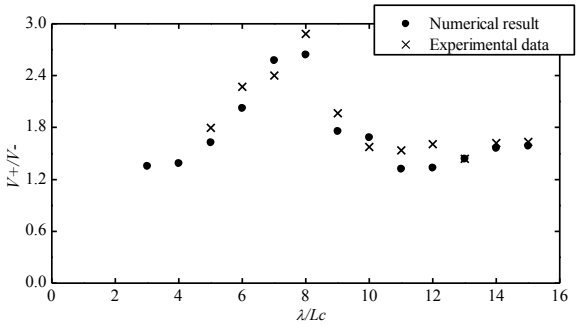

Fig. 15 Comparison of numerical and experimental results of the ratio of horizontal positive and negative velocities for the cube as a function of relative wave length

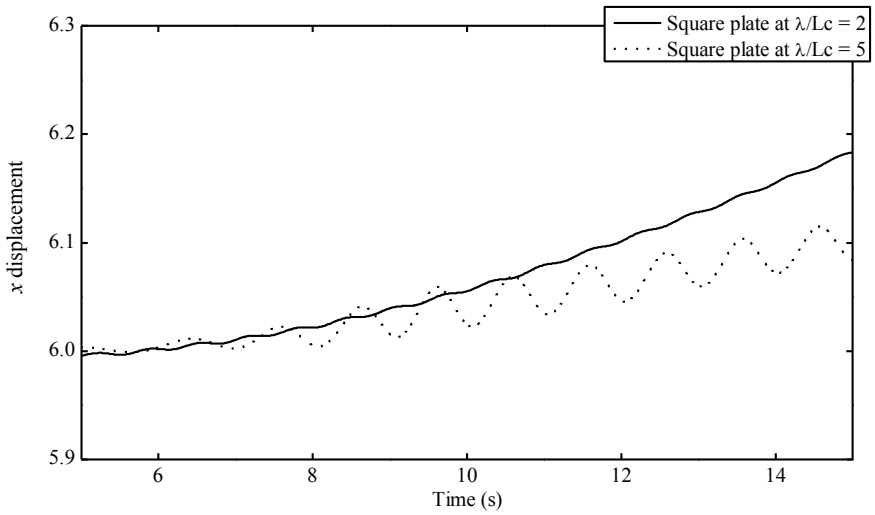

Fig. 16 Numerical result of displacement in the x direction for the square plate at $\lambda/L_c = 2$ and 5

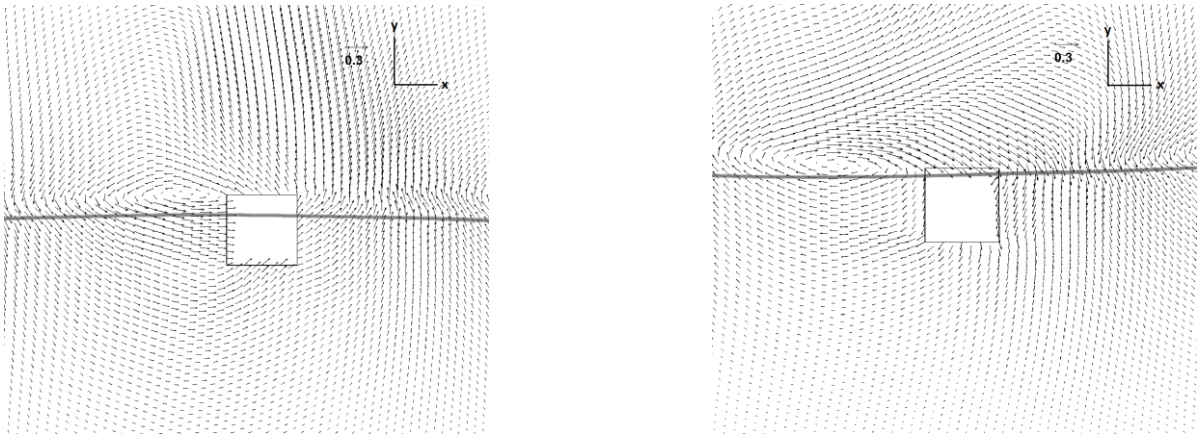

(a) t = 10.3s (b) t = 10.9s

Figure. 17 Velocity field around the cube with λ/L_c = 13 and H = 0.052m at two time instants: (a) t = 10.3s and (b) t = 10.9s

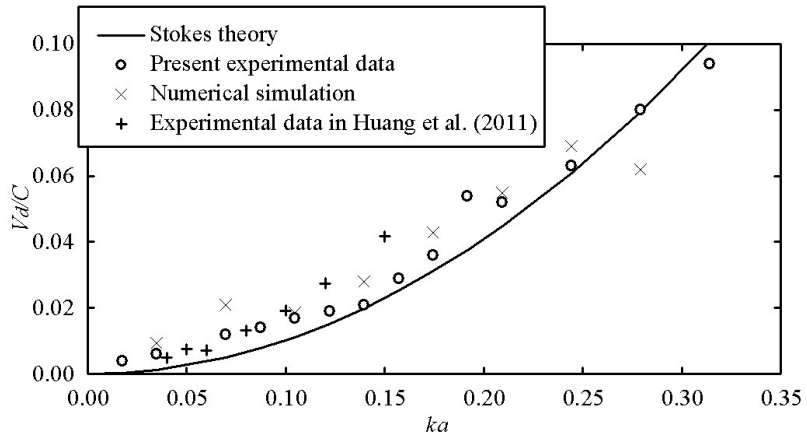

Fig. 18 Numerical result of drift velocity for the square plate and comparison with the experimental results of both the present study and Huang et al. (2011)

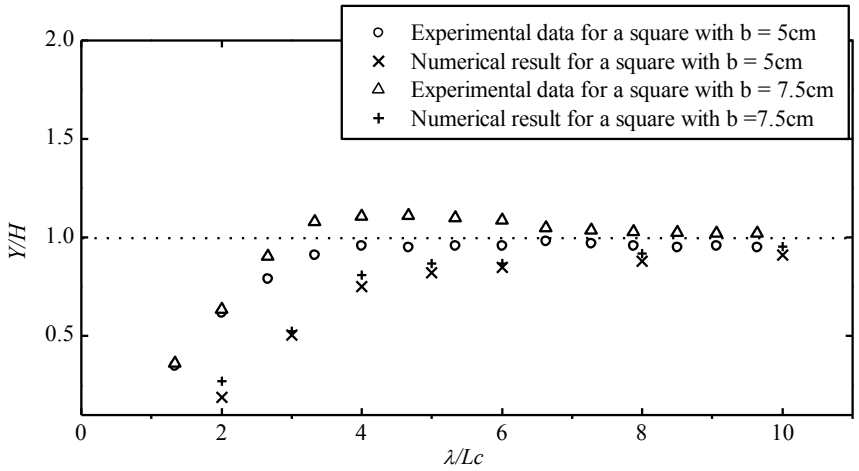

Fig. 19 Numerical and experimental heave RAOs for the square plate with two different thicknesses, b = 5cm and b = 7.5cm

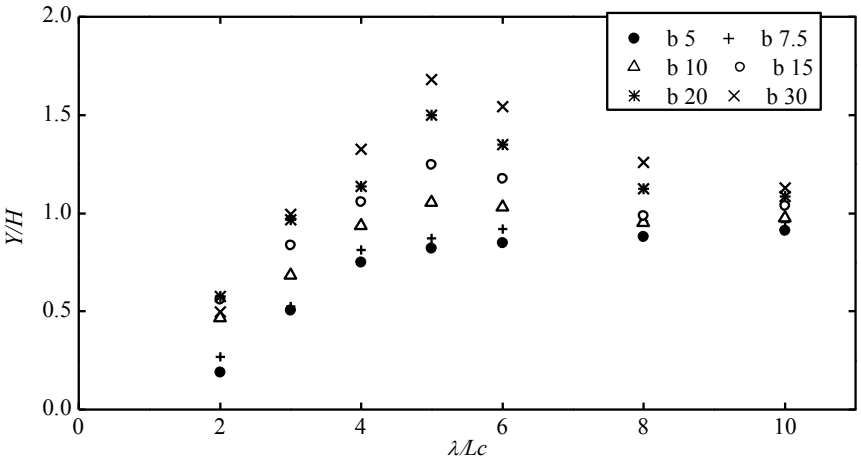

Fig. 20 Numerical result of heave response of square plates with variable floe thicknesses b

842

843 Table 1 Summary of OpenFOAM® simulations

844

Number of runs	λ(m)	H(m)	H/λ	λ/L_c
Cubic model (L_c = 20) with different wavelengths				
11	1 to 3.0	0.02 to 0.06	0.02	5 to 15
Square plate (L_c = 30 b = 5) with different wavelengths				
12	0.4 to 3.0	0.0176 to 0.132	0.044	1.333 to 10
Triangle plate (L_c = 30 b =5) with different wavelengths				
8	0.4 to 2.6	0.0176 to 0.1144	0.044	1.333 to 8.667
Square plate (L_c = 30 b = 5) with different wave heights				
8	1.8	0.02 to 0.16	0.0111 to 0.0899	6
Square plate (L_c = 30cm) with different thickness b = 7.5, 10, 15, 20, 30cm				
4	0.8	2.0	0.15	0.02

845

846

847